Soft Matter

Volume 1 | Number 1 | Jan 2013 | Pages 1–100

Soft Matter

www.rsc.org/softmatter

ROYAL SOCIETY OF CHEMISTRY

www.rsc.org/softmatter

ROYAL SOCIETY
OF CHEMISTRY

Soft Matter

Paper

Polymerized Ionic Liquid Diblock Copolymers: Impact of Water/Ion Clustering on Ion Conductivity

Jacob R. Nykaza,[a] Yuesheng Ye,[a] Rachel Nelson,[a] Aaron C. Jackson,[b] Frederick L. Beyer,[b] Eric M. Davis,[c] Kirt Page,[d] Sharon Sharick,[e] Karen I. Winey,[e] and Yossef A. Elabd[f] †

Herein, we examine the synergistic impact of both ion clustering and block copolymer morphology on ion conductivity in two polymerized ionic liquid (PIL) diblock copolymers with similar chemistries but different side alkyl spacer chain lengths (ethyl versus undecyl). When saturated in liquid water, water/ion clusters were observed only in the PIL block copolymer with longer alkyl side chains (undecyl) as evidenced by both small-angle neutron scattering and intermediate-angle X-ray scattering, i.e., water/ion clusters form within the PIL microdomain under these conditions. The resulting bromide ion conductivity in the undecyl sample was higher than the ethyl sample (14.0 mS cm^{-1} versus 6.1 mS cm^{-1} at 50 °C in liquid water) even though both samples had the same block copolymer morphology (lamellar) and the undecyl sample had a lower ion exchange capacity (0.9 meq g^{-1} versus 1.4 meq g^{-1}). No water/ion clusters were observed in either sample under high humidity or dry conditions. The resulting ion conductivity in the undecyl sample with lamellar morphology was significantly higher in the liquid water saturated state compared to the high humidity state (14.0 mS cm^{-1} versus 4.2 mS cm^{-1}), whereas there was no difference in ion conductivity in the ethyl sample when comparing these two states. These results show that small chemical changes to ion-containing block copolymers can induce water/ion clusters within block copolymer microdomains and this can subsequently have a significant effect on ion transport.

Introduction

Polymerized ionic liquids (PILs) are polymers containing covalently attached ionic liquid moieties that possess unique physiochemical properties, such as high solid-state ionic conductivity, high chemical and electrochemical stability, and widely tunable physical properties through ion exchange.[1-4] More specifically, PIL block copolymers have been synthesized by several research groups[5-7] and combine the properties of PILs and block copolymers, where the latter is known to self-assemble into a variety of different nanostructures (e.g., body centered cubic spheres, hexagonal packed cylinders, lamellae).[8] Researchers have shown that when PILs self-assemble into continuous ion-rich microdomains within

block copolymer morphologies, accelerated ion transport within continuous nanostructured ion-channels occurs.[9] Among PIL block copolymers, several studies have investigated imidazolium-based PIL block copolymers[10-14] due to their interest in a variety of applications, including anion exchange membranes (AEMs) for solid-state alkaline fuel cells (AFCs). However, to date, investigations of anion transport-morphology relationships in AEMs are not nearly as well explored as cation transport-morphology relationships in sulfonated proton exchange membranes (PEMs), where the latter investigations have had a significant impact on the design of PEMs for enhanced hydrogen fuel cell performance.[15]

Nafion, the most frequently investigated PEM, possesses a phase separated morphology with ion-rich and ion-poor domains.[16,17] The ion-rich domains are commonly referred to as ion clusters and when hydrated, these domains are connected and continuous throughout the membrane to allow for facile proton transport. In addition to Nafion, similar self-assembled connected continuous ion cluster morphologies have been observed in various PEMs, which have been achieved with various polymer chain architectures (e.g., graft copolymers, block copolymers).[18-22] Recently, this was clearly evidenced in work by Balsara and coworkers[23] in their study on a PEM triblock copolymer of polystrenesulfonate-block-polyethylene-block-polystyrenesulfonate in both humid air and liquid water (fully saturated). Ion/water-rich channels were observed with scanning transmission electron microscopy within the polystyrenesulfonate

a. Department of Chemical and Biological Engineering, Drexel University, Philadelphia, Pennsylvania 19104, United States
b. Army Research Laboratory, Aberdeen Proving Ground, Maryland 21005, United States
c. Department of Chemical and Biomolecular Engineering, Clemson University, Clemson, South Carolina 29634, United States
d. Materials Science and Engineering Division, National Institute of Standards and Technology, Gaithersburg, Maryland 20899, United States
e. Department of Materials Science and Engineering, University of Pennsylvania, Philadelphia, Pennsylvania 19104, United States
f. Department of Chemical Engineering, Texas A&M University, College Station, Texas, 77845
† To whom correspondence should be addressed; E-mail: elabd@tamu.edu.
Electronic Supplementary Information (ESI) available: Background calculations and SAXS data. See DOI: 10.1039/x0xx00000x

microdomain under fully saturated conditions, but not under humid conditions. Interestingly, proton conductivity in the fully saturated state was four times higher compared to the humid condition, suggesting that the ion/water channels within the microdomains of the block copolymer impact ion transport. Generally, when ion clustering is observed using X-ray scattering or various microscopic techniques, the ion conductivity improves compared to similar non-clustering PEMs.[24] It is important to note that ion clusters can cause a large activation barrier for intercluster hopping, which may hinder ion conductivity in select polymers. Beers and Balsara[25] suggested tailoring molecular weights to decrease domain sizes in block copolymers to prevent ion clustering, which in turn improved proton conductivity in their materials. Ion clustering has recently been observed in AEMs, including comb,[26] graft,[27] and aromatic[28] polymers with the design goal of improving ion conductivity. Hickner and coworkers[28] observed ion clustering in quaternary functionalized benzylmethyl-containing poly(arylene ether ketone)s (QA-PAEKS) with small-angle X-ray scattering. The QA-PAEKS AEMs possessed higher bromide conductivity than a randomly functionalized quaternary ammonium Radel (QA-Radel) AEM, where no ion clustering was observed in the latter AEM.

Along with the improvement of ion conductivity through ion clustering, the use of block copolymers to enhance ion conductivity in AEMs has also been explored similar to previous analogous studies in PEMs. Several recent reports[9, 18, 29-32] are examples of water-assisted ion transport in block copolymers for alkaline fuel cells. Recent work in our laboratory investigated the bromide and hydroxide conductivity in a PIL diblock copolymer poly(MMA-*b*-MEBIm-Br (or OH)) or poly(methyl methacrylate-*b*-1-[(2-methyacryoyloxy)ethyl]-3-butylimidazolium bromide or hydroxide).[9] In this previous work, the PIL block copolymer showed higher bromide and hydroxide conductivity (over an order of magnitude) than its analogous PIL random copolymer at a similar ion exchange capacity (IEC; 1.4 meq/g) and similar water uptake over a temperature range of 30 °C to 80 °C at high humidity (90% RH). The strong microphase separation (lamellae) in the PIL block copolymer was the hypothesized reason for the increase in conductivity, whereas no microphase separation was evident in the PIL random copolymer. Other PIL block copolymers have also been explored in our laboratory, where the block copolymer morphology (*e.g.*, morphology type, strength of microphase separation) plays a role in ion transport.[9, 32, 33]

In this study, to understand the role of block copolymer morphology and specifically ion/water clustering within the block copolymer morphology, a systematic study between two different imidazolium-based PIL diblock copolymers with similar chemistries was performed. The primary difference between these two block copolymers is the side alkyl spacer chain length between the backbone and the covalently attached imidazolium group (see Fig. 1), where this spacer length can impact the formation of water/ion clusters.[9,32] These two polymers were compared at similar ion exchange capacities (IECs) of 1.4 meq/g and at similar PIL (ion conducting) contents (≈40 vol%). The morphology was carefully characterized under dry, highly humidified, and fully saturated (in

liquid water) conditions using small-angle neutron scattering (SANS), small- and intermediate-angle X-ray scattering (SAXS, IAXS), and transmission electron microscopy (TEM). The impact of these morphological differences on bromide ion conductivity was explored.

Experimental

Materials.

Acetonitrile (anhydrous, 99.8 %) was used as received from Sigma-Aldrich. Ultrapure deionized (DI) water with resistivity ≈16 MΩ cm was used as appropriate. The bromide conducting PIL diblock copolymers, poly(MMA-*b*-MEBIm-Br) and poly(MMA-*b*-MUBIm-Br), were previously synthesized and a detailed protocol of their synthesis is described elsewhere.[32-34] Fig. 1 shows the chemical structure of these two bromide-conducting PIL diblock copolymers investigated in this study, where both diblock copolymers consist of the same nonionic first component (methyl methacrylate, MMA) and a second IL-containing component or polymerized ionic liquid (PIL), where the only difference is the length of the alkyl side chain in the PIL, where the short (S) alkyl side chain corresponds to 1-[(2-methacyloyloxy)ethyl]-3-butylimidazolium bromide (MEBIm-Br) and the long (L) alkyl side chain corresponds to 1-[(2-methacyloyloxy)undecyl]-3-butylimidazolium bromide (MUBIm-Br). In Fig. 1, x = 2 corresponds to two carbons (ethyl) on the short (S) alkyl side chain and x = 11 corresponds to eleven carbons (undecyl)
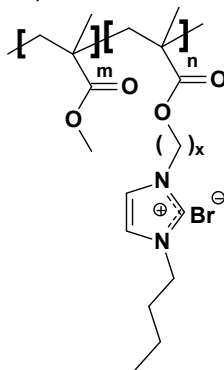

Fig. 1. Chemical structure of polymerized ionic liquid block copolymers. x = 2 corresponds to short (S) ethyl alkyl side chain length, poly(MMA-*b*-MEBIm-Br), and x = 11 corresponds to long (L) undecyl alkyl side chain length, poly(MMA-*b*-MUBIm-Br).

on the long (L) alkyl side chain. These two bromide-conducting PIL diblock copolymers can also be referred to as poly(MMA-*b*-MEBIm-Br) and poly(MMA-*b*-MUBIm-Br). A simplified naming system is proposed and used throughout this paper as shown in Table 1. For example, for L-1.4-59.3, L refers to the long alkyl side chain in the PIL, 1.4 refers to the ion exchange capacity (IEC) of the polymer in

meq/g, and 59.3 refers to the PIL composition in vol%. In this work, two long alkyl side chain block copolymers were synthesized for comparison with the short alkyl side chain length block copolymer. L-0.9-40.2 was synthesized for comparison with S-1.4-39.1 at the same PIL composition (≈40 vol%). Notice that the IEC in L-0.9-40.2 is lower due to the higher molecular weight of the PIL. L-1.4-59.3 was synthesized for comparison with S-1.4-39.1 at the same IEC. Notice the PIL composition (vol%) in L-1.4-59.3 is higher due to the higher molecular weight of the PIL. These comparisons are highlighted in bold text in Table 1. The physical properties of these PIL block copolymers are also listed in Table 1. The molecular weights of the samples were in a similar range of 20 kg mol^{-1} to 30 kg mol^{-1} and all PDIs were below 1.5. S-1.4-39.1 had two T_gs at 103 °C and 124 °C, corresponding to the PIL and PMMA domains, respectively, and both T_gs are similar to their respective homopolymer T_gs. L-0.9-40.2 and L-1.4-59.3 also possess two T_gs, where the same PMMA domain T_g was observed, while the T_g corresponding to the PIL domain is approximately 70 °C lower than S-1.4-39.1. The lower T_g of the PIL domain in the long alkyl chain samples is due to the increased alkyl chain length and is similar to its respective homopolymer T_g. The distinct two T_gs evidenced in the DSC data suggests that microphase separation occurs in all three samples.

PIL Block Copolymer Film Fabrication.
PIL block copolymer films were fabricated by first dissolving the polymer in anhydrous acetonitrile (10% by mass) and subsequently casting onto Teflon substrates (≈ 35 mm (*L*) × 4 mm (*W*) × 0.525 mm (*T*)) under ambient conditions for 24 h. The polymer films were then annealed under vacuum at 150 °C for 72 h. These annealed films were used to characterize physical properties. The film thicknesses, ranging between 100 μm to 200 μm, were measured with a Mitutoyo digital micrometer with ± 0.001 mm accuracy.

Characterization.
Vapor water uptake or content was measured with dynamic vapor sorption (DVS, TA Instruments Q5000). A dry sample of ≈1 mg was first loaded into the DVS and preconditioned at 0% RH and 30 °C for 2 h to remove any residual water in the sample. Only a small mass loss (< 0.5%) was observed during this 2 h period and the loss in mass did not change well before the end of this 2 h time period. The relative humidity was then systematically changed to a constant value at a fixed temperature or the temperature was systematically changed to a constant value at a fixed humidity and the film was allowed to equilibrate for 2 h at each condition. There was no change in mass prior to the end of this 2 h equilibration period, indicating that equilibrium water sorption was reached. The polymer water content [% by mass; g H_2O/ g dry polymer × 100] was calculated as follows:

$$W_{H_2O} = \frac{W - W_0}{W_0} \times 100$$

(1)

where W_0 and W are the dry and wet polymer masses (or weights) measured before and after the DVS experiment, respectively. The hydration number (λ), defined as the moles of water per mole of imidazolium cations in the hydrated polymer [mol H_2O/mol Im$^+$], was calculated using the following equation:

$$\lambda = \left[\frac{W_{H_2O}}{100}\right]\left[\frac{MW_{CP}}{MW_{H_2O}}\right]\left[\frac{1}{x_{PIL}}\right]$$

(2)

$$MW_{CP} = (1 - x_{PIL})MW_{MMA} + x_{PIL}MW_{PIL}$$

(3)

MW_{CP} is the molecular weight of the repeat unit of the copolymer and MW_{H_2O} and MW_{PIL} are of the molecular weights of water (18.02 g mol^{-1}) and PIL monomeric unit including counter anion (MW$_{PIL,MUBIm-Br}$ = 443 g mol^{-1} and MW$_{PIL, MEBIm-Br}$ = 317.23 g mol^{-1}) and x_{PIL} is the mole fraction of PIL unit in the block copolymer.

Saturated water uptake (*i.e.*, water uptake after soaking in liquid water) was measured by drying polymer samples for 24 h under vacuum at 25 °C and then recording the dry mass (Mettler AB54-S Analytical balance, accuracy ± 0.1 mg). Samples were soaked in a vial filled with DI water, where the temperature of the vial was controlled using a hot oil bath (Fisher Scientific Isotemp). Samples were removed after 2 h, the excess water on surface of film was gently removed with a lint-free cloth, and the mass was re-measured. At least three measurements were performed at each temperature. The error among repeated experiments was on average < 10%. Saturated water uptake and hydration values were calculated as described above in Eqs. 1 and 2.

The ionic (bromide) conductivities of the polymer films were measured with impedance spectroscopy (Solartron, 1260 impedance analyzer, 1287 electrochemical interface, Zplot software) over a frequency range of 1 Hz to 10^7 Hz at 300 mV. The in-plane conductivities of the PIL films were measured in a custom-made cell with four-parallel electrodes, where an alternating current was applied to the outer electrodes and the real impedance or resistance, *R*, was measured between the two inner reference electrodes. The resistance was determined from a high x-intercept of the semi-circle regression of the Nyquist plot. Conductivity was calculated by using the following equation: $\sigma = L/AR$, where *L* and *A* are the distance between two inner electrodes and the cross section area of the polymer film (*A = Wl*; *W* is the film width and *l* is the film thickness), respectively. Samples were allowed to equilibrate for 1 h at each condition followed by six measurements (one every ten minutes at each condition). The values reported are an average of these steady-state measurements. An average error of < 5% was observed between these multiple steady-state values and duplicate experiments. The temperature and relative humidity for film conductivities measured under water vapor conditions were controlled by placing the cell in an environmental chamber (Tenney, BTRS model). The temperature for film conductivities measured saturated in liquid water was controlled by placing the cell in a vessel heated by heating tape using a variable autotransformer (Power State), where the film in

Table 1. Polymerized Ionic Liquid Block Copolymer Properties.

Sample[a]	x[b]	PIL composition			IEC[f]	M_n[g]	M_n[h]	PDI	T_g[i]
		mol%[c]	wt%[d]	vol%[d,e]		(kg mol^{-1})	(kg mol^{-1})		(°C)
S-1.4-39.1	2	17.3	40.0	39.1	1.4	13.1+8.68	19.90	1.26	103, 124
L-0.9-40.2	11	12.3	38.3	40.2	0.9	19.8+7.76	26.45	1.26	23, 124
L-1.4-59.3	11	23.3	57.3	59.3	1.4	19.8+14.7	28.43	1.48	27, 125

[a]L and S correspond to long (x = 11) and short (x = 2) alkyl side chain length, respectively; first and second numbers correspond to ion exchange capacity (IEC; meq g^{-1}) and PIL composition (vol%), respectively. [b]Alkyl side chain length. [c]PIL composition (mol%) determined from ^{1}H NMR spectroscopy. [d]PIL composition (wt%). [e]PIL compositions (vol%) calculated from density of PMMA and PIL homopolymer (see Supporting Information for calculation). [f]IEC calculated as meq Im$^+$ per g of polymer (see Supporting Information for calculation). [g]Calculated from ^{1}H NMR spectra. [h]Determined by SEC. [i]Determined by DSC; midpoint method.

the cell was saturated in liquid water. The temperature of this vessel was monitored using a thermocouple (Omega 650 Type J).

Small angle X-ray scattering (SAXS) of samples under dry conditions was performed at Drexel University on a Rigaku S-MAX3000 pinhole SAXS camera with a 150 cm camera length. Cu-Kα X-rays were produced from a MicroMax-002+ Microfocus sealed tube X-ray source. The scattering data were collected using a Gabriel-type two-dimensional multiwire X-ray area detector. The isotropic 2-D scattering patterns were azimuthally integrated to yield 1-D intensity versus scattering angle (q) profiles. The intensities are reported in arbitrary units (a.u.). Data collection for each sample was conducted over 3 h in a through-plane orientation. Data analysis was performed using a Matlab-based Graphical User Interface (GUI). Morphologies were classified by taking the ratio of the positions of higher order X-ray scattering correlation peaks to the primary peak position, q^*, and comparing to known peak position ratios.

SAXS on samples under humidity- and temperature-dependent conditions was performed on a multi-angle X-ray scattering system at the University of Pennsylvania using a custom designed environmental chamber.[35] This system generates Cu-Kα X-rays, λ = 0.154 nm, from a Nonius FR 591 rotating anode operated at 40 kV and 85 mA. The bright, highly collimated beam was obtained *via* Osmic Max-Flux optics and pinhole collimation in an integral vacuum system. The scattering data were collected using a Bruker Hi-Star two-dimensional detector with a sample-to-detector distance of 150 cm. Room-temperature data was collected for 1 h for each block copolymer film along the through-plane and in-plane directions of the films. Data was analyzed using Datasqueeze software.[36] The intensities were first corrected for primary beam intensity, and then background scattering was subtracted. The isotropic 2-D scattering patterns were then azimuthally integrated to yield 1-D intensity versus scattering angle (q) profiles. The intensities are reported in arbitrary units (a.u.). Morphologies were classified by taking the ratio of the positions of higher order X-ray scattering correlation peaks to the primary peak position, q^*, and comparing to known peak position ratios.[37] Relative humidity (RH)

was varied by regulating the flow of compressed air mixed with water vapor into the chamber and the sample temperature was controlled by flowing heated or cooled water through the chamber walls, as well as varying the temperature of the water vapor. The error between the set values and measured values for relative humidity and temperature was minimized through a proportional-integral-derivative (PID) feedback loop. The environmental chamber accesses a temperature range of 25 °C to 90 °C with a precision of 0.05 °C to 0.5 °C and a humidity range of 0% RH to 95% RH with a precision of 1.5% RH at 30 °C and 3% RH at 80 °C. For *in situ* measurements, samples were equilibrated for at least 2 h at each condition before collecting X-ray scattering data.

Intermediate angle X-Ray scattering (IAXS) was also performed at the University of Pennsylvania with the same system described above. Samples under vacuum and at 90% RH were performed similarly to the SAXS experiments described above. For samples saturated in liquid water, films were soaked overnight in DI water prior to collecting X-ray scattering. The films were sandwiched between two polyimide films and sealed in custom-made sandwich cells to ensure that the block copolymer films remained saturated during the experiment. X-ray scattering from the sample was collected at ambient temperature under vacuum for 2 h. The scattering from two polyimide films, also collected at room temperature under vacuum for 2 h, was subtracted from the sample scattering prior to azimuthal angle integration.

Morphology of the S-1.4-39.1 sample was imaged previously with a transmission electron microscope (TEM) and the details of the sample preparation and experimental conditions can be found in a previous publication.[9] Morphology of the L-1.4-59.3 and L-0.9-40.2 samples was imaged at the U.S. Army Research Laboratory. Samples were prepared for TEM by ultracryomicrotomy. A Leica UCT ultramicrotome equipped with a cryogenic cooling stage was used to cut sections approximately 90 nm thick using a Microstar diamond knife. Samples were cooled to -10 °C prior to sectioning. A JEOL JEM-2100F TEM and a Gatan 806 high-angle annular dark field scanning TEM (HAADF STEM) detector were used to collect dark field data. The TEM was operated at 200 kV, with a 40 μm

condenser aperture, a HAADF STEM collection angle of 48 to 168 mrad, and spot size of 0.2 nm. Gatan Digital Micrograph was used to collect and analyze the data. In dark field images, high Z regions appear bright and low Z regions are dark.

Small-angle neutron scattering (SANS) experiments were performed on the NG-B 10m SANS, operated by the National Institute of Standards and Technology (NIST) nSoft 10 m consortium at the NIST Center for Neutron Research (NCNR). The incoming neutron wavelength was set to 5 Å and 12 Å for the collection of mid to high q and low q data, respectively. Furthermore, the sample-to-detector distance (SDD), as well as the detector offset, was varied to collect a range of q values for the two wavelength settings (q values ranging from 0.0035 Å^{-1} to 0.5 Å^{-1}). The total collection time for each sample was approximately 2 h. The samples were hydrated in liquid D_2O for at least 48 h prior to beginning scattering experiments. The use of D_2O as opposed to H_2O was necessary to achieve a high contrast between the samples and sorbed D_2O molecules, due to the high scattering length density (SLD) for the deuterium atom. Prior to beginning SANS experiments, the D_2O saturated samples were mounted in a zero-gap sample cell with quartz windows. SANS experiments were carried out at 25 °C, 50 °C, and 80 °C, where the temperature of the sample cells was kept constant using a temperature bath. After completion of the scattering experiments, the hydrated film thickness was measured using a micrometer. Film thicknesses were recorded as the average of at least three measurements on the sample. The measured intensity from SANS was converted to absolute intensity by correcting for transmission and background scattering. The SANS data were reduced using software developed at the NCNR.[38]

Results and discussion

Fig. 2 shows TEM and SAXS data for all three samples listed in Table 1. All samples were under vacuum for these experiments (*i.e.*, no measurable water present). Fig. 2a is a bright field TEM image of S-1.4-39.1, which has previously been published.[9] The image shows a lamellar morphology. This morphology type is supported by the SAXS profile of S-1.4-39.1 shown in Fig. 2d, where four well-defined scattering peaks at $q*$ (primary), $2q*$, $3q*$, and $4q*$ were observed and these peak locations are indicative of a periodic lamellar morphology. A Bragg spacing of 25.1 nm for S-1.4-39.1 was determined from the SAXS data using the following equation, d = $2\pi/q*$.

Fig. 2b shows an HAADF STEM image of L-0.9-40.2 (a comparison to S-1.4-39.1 at a similar PIL composition, but lower IEC), in which a lamellar morphology was also observed, similar to that of S-1.4-39.1. Fig. 2d shows the corresponding SAXS profile for this sample, where three well-defined scattering peaks at positions $q*$, $2q*$, and $4q*$ were observed, indicative of a lamellar morphology. A Bragg spacing of 27.9 nm was calculated from the SAXS data for this sample. Therefore, an increase in alkyl chain length results in a similar lamellar morphology when the PIL volume fraction is similar (different IEC; 1.4 meq g^{-1} versus 0.9 meq g^{-1}), but an increase in lamellar period of ≈2.8 nm was observed from S-1.4-39.1 to L-0.9-40.2.

Fig. 2c shows the HAADF STEM image of L-1.4-59.3 (a comparison to S-1.4-39.1 at a similar IEC, but higher PIL composition). Although L-1.4-59.3 has the same IEC as S-1.4-39.1, the increase in PIL content (59.3 vol% versus 40.2 vol%) results in a change from lamellae to PMMA cylindrical domains within a continuous PIL matrix. Fig. 2d shows the SAXS profile of the L-1.4-59.3 sample, where only two broad peaks at $q*$ and $2q*$ were observed.
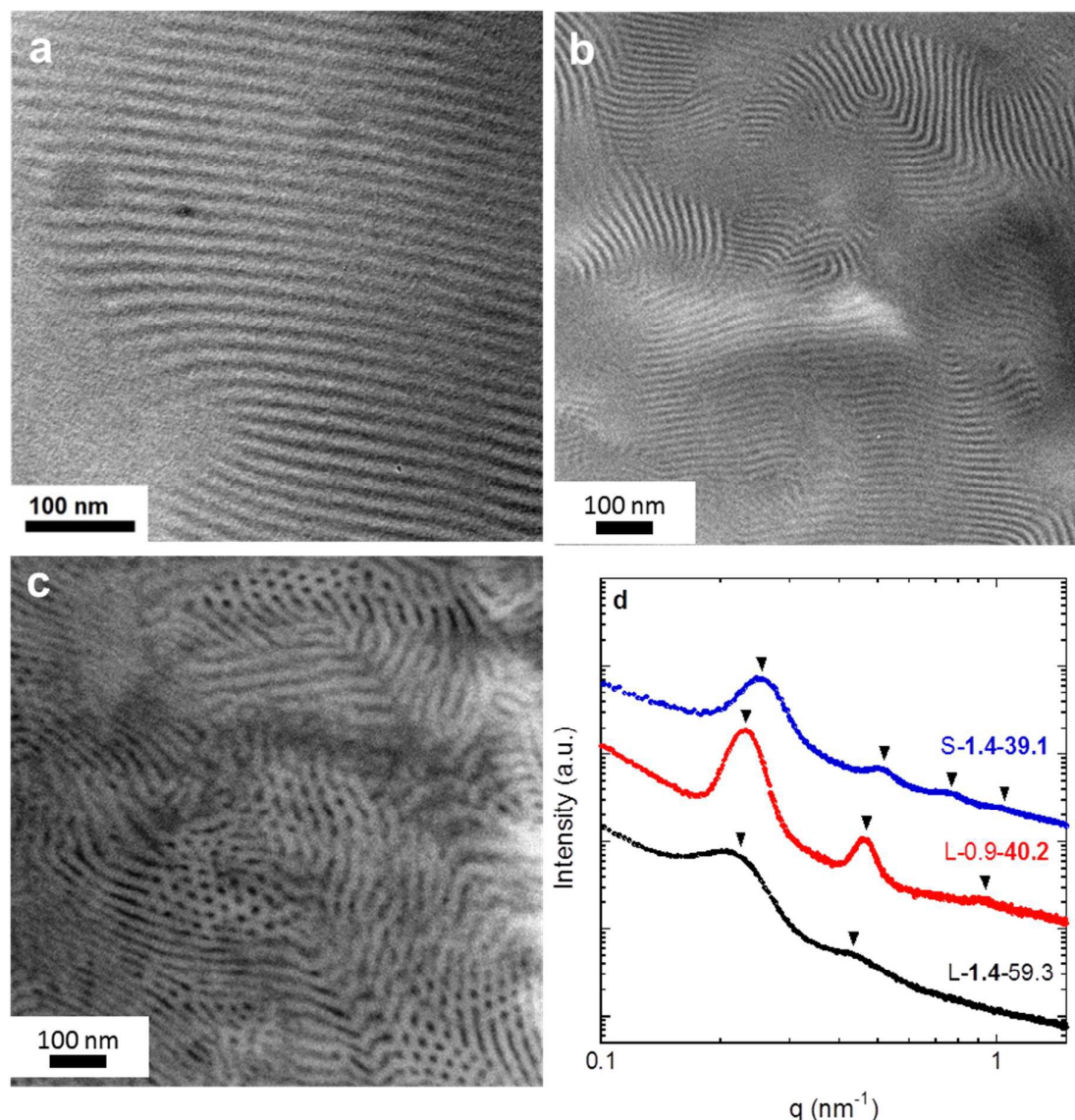
Soft Matter

Fig. 2. Electron microscopy images of PIL block copolymers at room temperature under vacuum: (a) S-1.4-39.1 [ref. 9], (b) L-0.9-40.2, (c) L-1.4-59.3. (a) bright-field TEM, samples unstained; dark regions correspond to PIL domains. (b) and (c) HAADF STEM; sample unstained; light regions correspond to PIL domains. (d) Small-angle X-ray scattering profiles. SAXS data collected at 25 °C under vacuum. Arrows indicate peak positions. Data are vertically offset for clarity.

Fig. 3 shows a comparison of humidity-dependent ion conductivity and hydration values of the PIL block copolymers at 50 °C. Measurements were conducted at various humidities ranging from 30% RH to 90% RH (circles) and in liquid water (square). Additionally, the humidity-dependent data were extrapolated to 100% RH (dashed line) for comparison with the measured liquid water results; both correspond to a water activity of one. Fig. 3a shows the ionic conductivity of S-1.4-39.1, and as expected, the bromide conductivity increases over three orders of magnitude with increasing RH. This increase can be attributed to a water-assisted transport mechanism, where an increase in hydration

number (λ = 1-7 mol water/mol Im$^+$; Fig. 3b) was observed over this humidity range. Interestingly, when the results were extrapolated to 100% RH to compare with samples measured in liquid water, there was a discontinuous increase in the hydration number of ≈17% even though no increase in bromide conductivity was observed. Similarly, the bromide conductivity of L-0.9-40.2 increases over three orders of magnitude with increasing RH as shown in Fig. 3c. However, when extrapolated to 100% RH and compared to measurements in liquid water, an increase in bromide conductivity of ≈233% (4.2 mS cm^{-1} versus 14.0 mS cm^{-1}) was observed. The large change in conductivity can be attributed to the increase in hydration number of L-0.9-40.2 by ≈113% from the extrapolated 100% RH value to the measure liquid water value as shown in Fig. 3d. It is important to note that L-0.9-40.2 had similar conductivities compared to S-1.4-39.1 over the studied humidity range, even though it has a lower IEC (0.9 meq g^{-1} versus 1.4 meq g^{-1}), slightly lower hydration numbers, and a similar lamellar morphology. However, when comparing the liquid water conductivities of L-0.9-40.2 to S-1.4-39.1, a ≈130% increase in conductivity (14.0 mS cm^{-1} versus 6.1 mS cm^{-1}) was observed. Note that there is a difference in the liquid water hydration numbers (13.8 mol H$_2$O/mol Im$^+$ versus 10.2 mol H$_2$O/mol Im$^+$) when comparing L-0.9-40.2 to S-1.4-39.1, but this may not be the sole factor affecting the conductivity.

Interestingly, the large discontinuity in conductivity that was observed for L-0.9-40.2 between the extrapolated 100% RH value and the measured liquid water value was not observed for L-1.4-59.3 (see Fig. 3e) even though an even larger increase in the hydration number of ≈221% from the extrapolated 100% RH value and the measured liquid water value was observed (see Fig. 3f). Similar to the two previous samples, the bromide conductivity of L-1.4-59.3 increases three orders of magnitude over the humidity range studied. Note the L-1.4-59.3 has a slightly higher conductivity than S-1.4-39.1 with a lower hydration value over the humidity range studied. Similar to L-0.9-40.2, a ≈97% increase in the liquid water bromide conductivity (12.0 mS cm^{-1} versus 6.1 mS cm^{-1}) was observed when comparing L-1.4-59.3 to S-1.4-39.1. Note that a more significant increase in liquid water hydration number (22.5 mol H$_2$O/mol Im$^+$ versus 10.2 mol H$_2$O/mol Im$^+$) was observed when comparing L-1.4-59.3 to S-1.4-39.1. This result was unexpected since both polymers have the same IEC of 1.4 meq g^{-1}, *i.e.*, same concentration of hydrophilic charged groups. To understand these results in greater detail, the morphologies of the samples were explored in liquid water and at various humidities and at various temperatures.

Note that in other ionomers, such as Nafion, a discontinuity between 100% RH and liquid water hydration numbers has been observed (14 versus 22).[39] Some researchers have suggested that results from water vapor are collected in a non-equilibrium state, where measurements over longer time scales result in the hydration number at 100% RH increasing and approaching the value of the liquid water hydration number.[40]
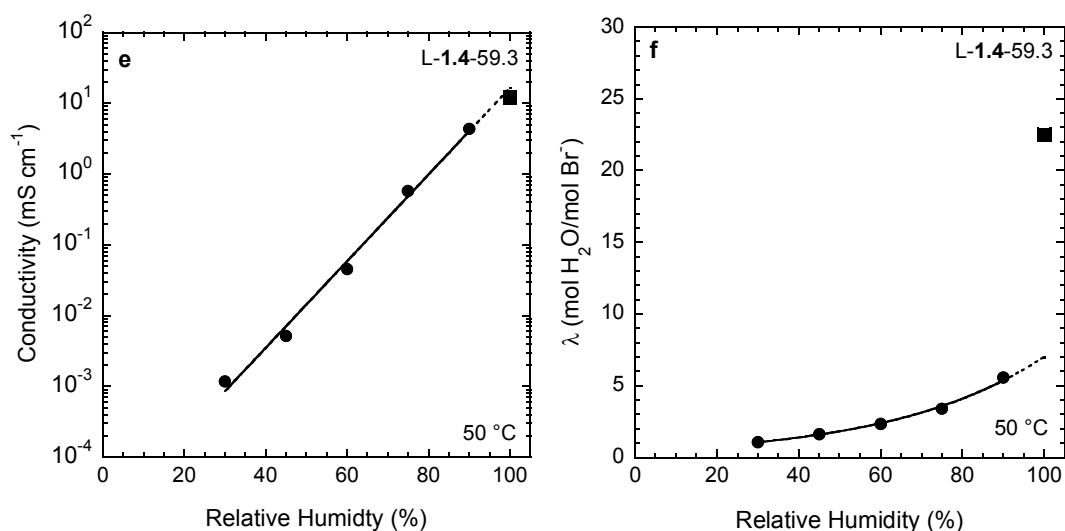
Soft Matter

Paper
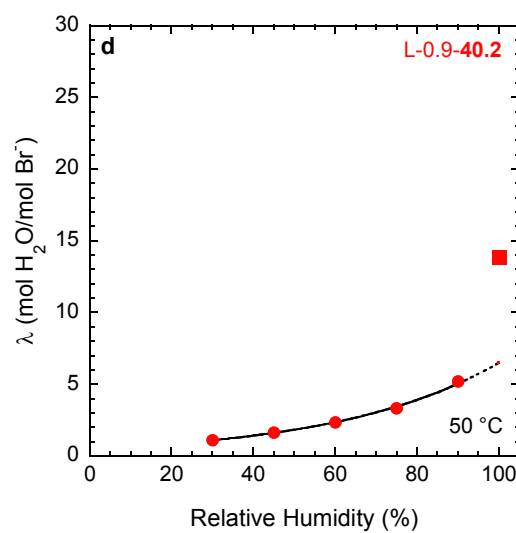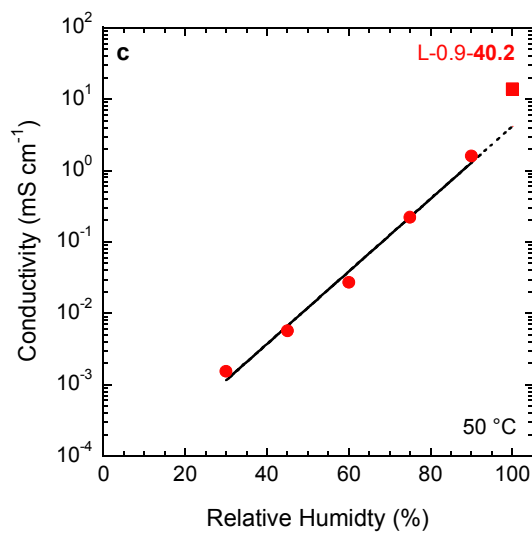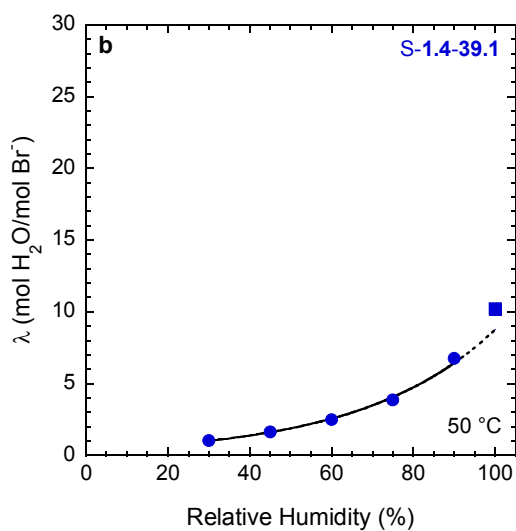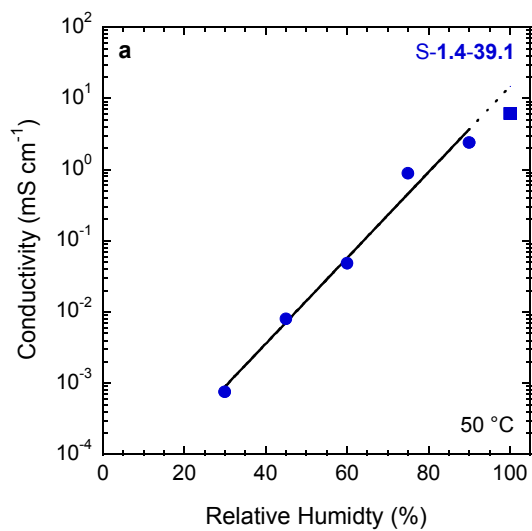
Fig. 3. Bromide ion conductivity (a,c,e) and hydration number (b,d,f) at 50 °C for the PIL block copolymers: (a,b) S-1.4-39.1 (blue), (c,d) L-0.9-40.2 (red), and (e,f) L-1.4-59.3 (black). Solid lines represent trend line of the data, and the dashed line represents an extrapolation of that trend to 100% RH. The squares represent the measured bromide ion conductivities and hydration numbers at 50 °C saturated in liquid water.

First, the morphologies of the PIL block copolymers were examined by SANS and IAXS saturated in liquid D_2O and H_2O, respectively. Fig. s 4a, 4b, and 4c show SANS profiles of S-1.4-39.1, L-0.9-40.2, and L-1.4-59.3, respectively, saturated in liquid D_2O at 25 °C, 50 °C, and 80 °C. The SANS profile for S-1.4-39.1 (see Fig. 4a) has two well-defined scattering peaks with positions q^* (primary peak) and $3q^*$, suggestive of a microphase separated lamellar morphology. There is no observed shift in the primary peak position at elevated temperatures indicating that the morphology remains stable over the temperature window explored with no measureable increase in lamellar period. Note that q^* in Fig. 4a is lower compared to the dry SAXS results in Fig. 2d, corresponding to an increase in lamellae period due to the presence of D_2O in the system. Similar to S-1.4-39.1, L-0.9-40.2 displayed a lamellar morphology under dry conditions (SAXS data in Fig. 2d), however the SANS result only displays a primary peak, q^*, in Fig. 4b and this peak position does not change with increasing temperature.

Interestingly, the presence of an additional correlation peak at high q (≈1.53 nm^{-1}) was observed in L-0.9-40.2, but not in S-1.4-39.1. This peak also shifts to lower q and broadens as the temperature increases from 25 °C to 80 °C. The presence of this new peak indicates there is additional morphological feature in L-0.9-40.2, but on a smaller length scale than the d-spacing of the block copolymer lamellar morphology. The q value (at 25 °C) correlates to a d-spacing of 4.1 nm and increases to 5.9 nm as temperature increases. This result would suggest that an increase in the length of the alkyl side chain of L-0.9-40.2, compared to S-1.4-39.1, allows for the cationic moieties on the longer alkyl chains to cluster within the microphase separated PIL microdomains, forming water/ion clusters.

A similar high q correlation peak has been observed in the scattering profiles of other ion exchange membranes of comparable

structural form, such as Nafion, where sulfonic acid groups on the perfluoroether side chains of Nafion coalesce to form ionic clusters (3 nm to 5 nm) and ultimately, interconnected ionic domains (Gierke model).[38, 41] It is thought that these interconnected ionic structures allow for more facile water and proton transport.[42] The correlation peak for the ionic domains in Nafion is located in a similar location as the correlation peak at high q for L-0.9-40.2 and suggests water/ion clusters with an intercluster distance on the order of 5 nm. Additionally, the shift of the correlation peak to lower q value can be indicative of an increase in cluster size with increasing temperature, while the broadening of this peak signifies that the size disparity of the clusters in L-0.9-40.2 is increasing (*i.e.*, greater variation in size between the individual water/ionic domains). The high conductivity value in this material suggests that these water/ion clusters are connected throughout the film.

Similar to Fig. 4b, L-1.4-59.3 shows the presence of a correlation peak at high q, where this peak shifts to lower q and broadens as temperature is increased from 25 °C to 80 °C as seen in Fig. 4c. Again, this correlation peak is indicative of water/ion clusters with a correlation distance on the order of 5 nm, enabled by the increased length of the alkyl portion of the side chain. The SANS results show an additional peak at $2q^*$ for L-1.4-59.3, which was not observed for L-0.9-49.2, possibly due to the differences in morphology types. Table 2 summarizes the SANS results: the primary peak positions (q^*), water/ionic cluster peak positions (q^i), and corresponding Bragg spacings.

IAXS experiments on the block copolymer materials saturated in liquid H_2O (Fig. 4d) were also conducted to compliment the SANS results. The IAXS data confirm the presence of a correlation peak at high q for only the long alkyl side chain samples and not the short alkyl side chain sample, suggesting there are water/ion clusters. The peaks in Fig. 4d at lower q are due to the higher ordering scattering

peaks due to block copolymer microphase separation, also seen in Fig. 2d.

The samples were also examined under vacuum and at 90% RH (Fig. 5) to determine if these water/ion clusters are present without liquid water. Interestingly, at both vacuum and 90% RH conditions, the correlation peak at ≈1.4 nm^{-1} is not present in any of the materials contrary to what was observed exclusively for the long alkyl side chain samples saturated in liquid water. This finding provides a rationale for the observed results in Fig. 3, where the ion conductivity of L-0.9-40.2 increases significantly from the extrapolated 100% RH value to the measured liquid water value. Also, the formation of water/ion clusters explains why the conductivity of L-0.9-40.2 is higher than S-1.4-39.1 (14.0 mS cm^{-1} versus 6.1 mS cm^{-1}) at 50 °C in liquid water even though it has a lower IEC. The large increase in hydration number for both long alkyl side chain samples when saturated in liquid water compared

to the extrapolated 100% RH value may also be attributed to formation of water/ion clusters within the PIL microdomains allowing the samples to absorb more water. The S-1.4-39.1 sample does not exhibit this additional clustering resulting in similar conductivity and hydration between the fully humidified and liquid conditions. Unlike L-0.9-40.2, a discontinuity in the ion conductivity for L-1.4-59.3 from the extrapolated 100% RH value to the measured liquid water value was not observed even though the water/ion clusters were detected for this sample in liquid water. L-1.4-59.3 also differs from L-0.9-40.2 in that it has a continuous network morphology, where additional ion/water clusters may not significantly impact the ion conductivity compared to the confinement of ion/water clusters within lamellar microdomains, as was observed in L-0.9-40.2.
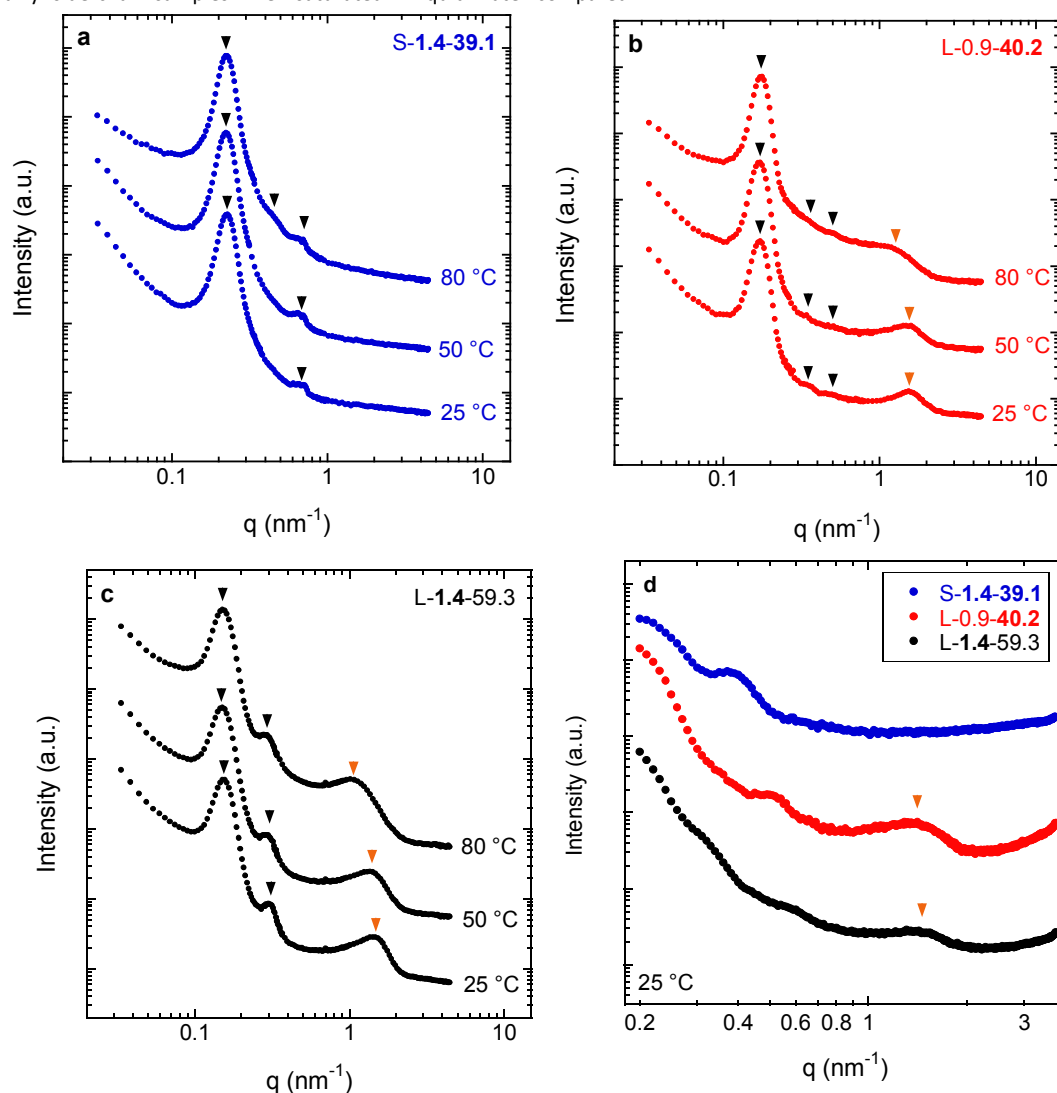
Fig. 4. Small-angle neutron scattering (SANS) (a,b,c) at 25 °C, 50 °C, and 80 °C saturated in liquid D_2O and intermediate-angle X-ray scattering (IAXS) (d) at 25 °C saturated in liquid H_2O. Black and orange arrows indicate peak positions associated with block copolymer microphase-separated morphology and ion clustering, respectively. Data are vertically offset for clarity.

Table 2. SANS Results.

Sample	Temp. (°C)	q^* (nm^{-1})	d^* (nm)[a]	q^i (nm^{-1})	d^i (nm)[b]
S-1.4-39.1	25	0.22	28.6	--	--
	50	0.22	28.6	--	--
	80	0.22	28.6	--	--
L-0.9-40.2	25	0.17	37.0	1.53	4.1
	50	0.17	37.0	1.41	4.5
	80	0.17	37.0	1.07	5.9
L-1.4-59.3	25	0.15	41.9	1.53	4.1
	50	0.15	41.9	1.36	4.6
	80	0.15	41.9	1.01	6.2

[a]Correlation distance calculated by $d^* = 2\pi/q^*$, where q^* is the position of the primary peak obtained from 1-D SANS data; [b]Correlation distance calculated by $d^i = 2\pi/q^i$, where q^i is the position of the water/ion cluster peak obtained from 1-D SANS data.
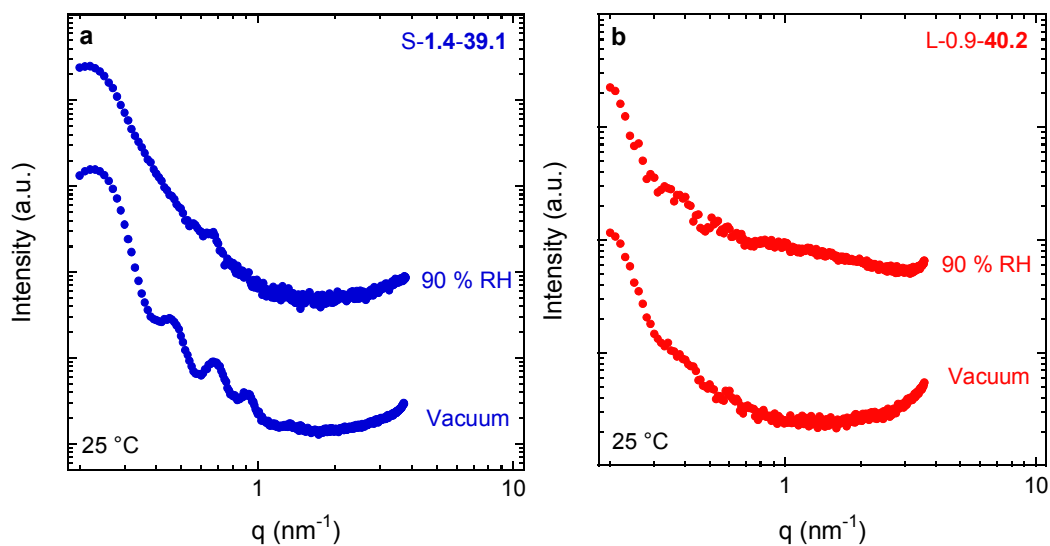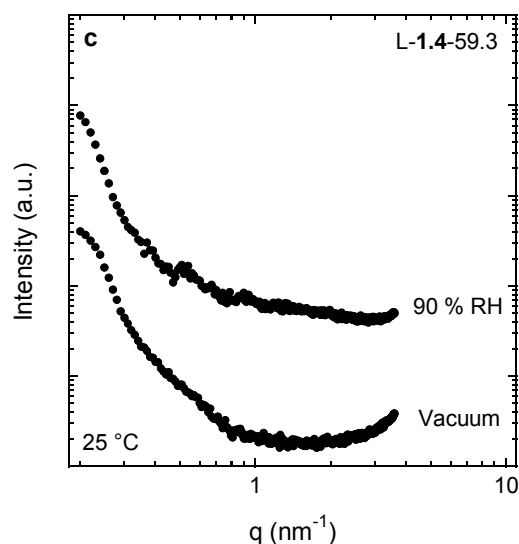
Fig. 5. Intermediate-angle X-ray scattering (IAXS) results of PIL block copolymers: (a) S-1.4-39.1 (blue) (b) L-0.9-40.2 (red) and (c) L-1.4-59.3 (black) at 25 °C under vacuum and 90% RH. Data are vertically offset for clarity.

In addition to the impact of liquid water on conductivity and morphology of these PIL block copolymers, the conductivity and morphology were explored as a function of temperature at high humidity, where these are conditions of interest for applications such as alkaline fuel cells. Fig. 6a shows bromide ion conductivity at 90% RH as a function of temperature for all PIL block copolymers. At all temperatures studied, L-1.4-59.3 has a higher conductivity than S-1.4-39.1 even though L-1.4-59.3 has a lower water uptake and corresponding hydration number (see Fig. 6b). Note that the block copolymer morphology type (lamellae or PMMA cylinders) of each sample does not change from dry to 90% RH or with increasing temperature at 90% RH as evidenced by X-ray scattering (Supporting Information Fig. S1-S2). This unusual behavior of higher ion conductivity at lower water contents may be due to a difference in morphology types between the two samples, where L-1.4-59.3 has a cylindrical morphology (see Fig. 2c) in which the PIL or conducting phase is the majority phase (*i.e.*, continuous) compared to S-1.4-39.1, which has a lamellar morphology (see Fig. 2a). More surprisingly, L-0.9-40.2 has a higher conductivity than S-1.4-39.1 at temperatures ≥ 60 °C even though L-0.9-40.2 has a lower IEC (0.9 meq g^{-1} vs. 1.4 meq g^{-1}) and lower hydration number (5 mol H$_2$O per mol Im$^+$ vs. 8 mol H$_2$O per mol Im$^+$) than S-1.4-39.1 and both samples have a similar lamellar morphology type (see Fig. s 2b And 2a). These results suggest that the longer alkyl chain length provides a more favorable configuration for imidazolium cations within the microphase separated PIL domain and contributes to a more efficient organization of water and ions, even with the absence of ion clusters. Also, note that the bromide conductivities in all polymers follows an Arrhenius behavior with temperature at high humidity promoted by the thermal activation of water-assisted ion transport.[43] The activation energies for L-0.9-40.2 and L-1.4-59.3 are 96.6 kJ mol^{-1} and 86.2 kJ mol^{-1}, respectively, which are both approximately three times higher than S-1.4-39.1 at 26.7 kJ mol^{-1}. These activation energies are within range of those reported for imidazolium-bromide ionic liquid-water mixtures.[44]
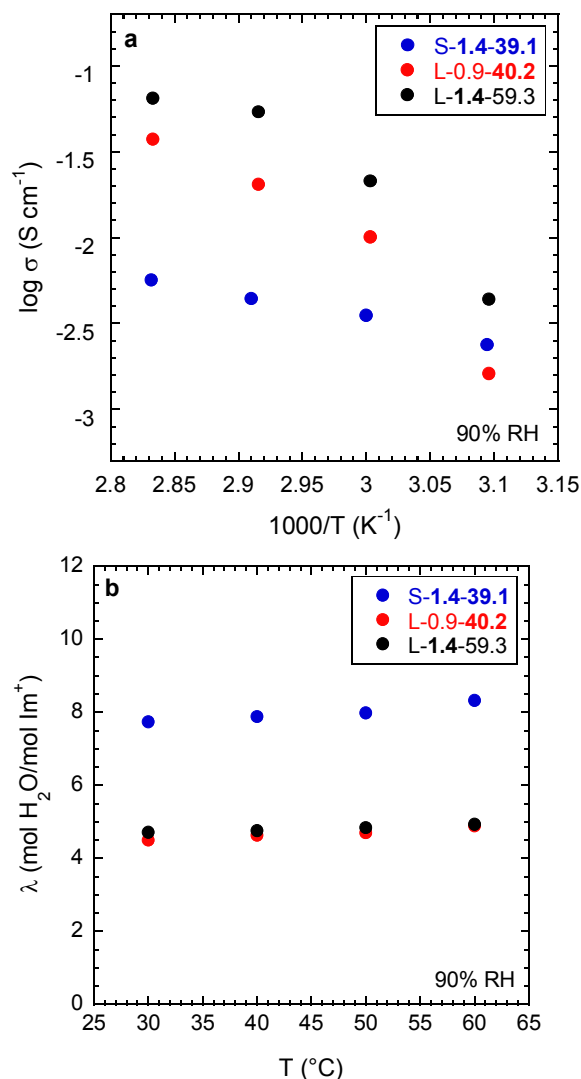
Fig. 6. Temperature-dependent properties at 90% RH: (a) bromide ion conductivity and (b) normalized water content (hydration number)

Conclusions

The synergistic impact of water/ion clustering and block copolymer morphology on ion conductivity was explored through a systematic study of two PIL block copolymers with different alkyl side chain lengths (ethyl versus undecyl). The undecyl sample was compared to the ethyl sample at the same PIL content (≈40%) and IEC (1.4 meq g^{-1}). The morphologies of the samples in the dry, hydrated, and liquid saturated states were carefully characterized with SANS, SAXS, IAXS, and TEM. Ion transport and water uptake were measured with impedance spectroscopy and dynamic vapor sorption, respectively. A key result from this study is the formation of water/ion clusters in the undecyl samples when saturated in liquid water as observed by SANS and IAXS. Water/ion clusters were not observed in the ethyl samples under any condition and were not observed in the undecyl samples under highly humidified or dry conditions. The formation of water/ion

clusters was only observed in the undecyl samples saturated in liquid water.

In this study, water/ion clusters within PIL microdomains appear to have a significant impact on ion transport, where increases in bromide ion conductivity in the liquid water saturated state were observed when the undecyl sample was compared to the ethyl sample at the same lamellar morphology even though the undecyl sample had a lower IEC. An increase in bromide ion conductivity was also observed in the undecyl sample with lamellar morphology when comparing the liquid water state to the high humidity state. Both of these results indicate the beneficial impact of water/ion cluster formation within PIL microdomains on ion transport. Furthermore, the improvement in conductivity suggests that the water/ion clusters are percolated and possess sufficient local mobility to facilitate ion transport across the membrane.

When comparing the undecyl sample to the ethyl sample at the same IEC, the undecyl sample also had higher bromide ion conductivity in the liquid water saturated state. However, in addition to water/ion clusters exclusive to the undecyl sample in this saturated state, a block copolymer morphology change from lamellar to PMMA cylinders inside of continuous PIL microdomains was observed due to the increase in PIL composition. Unexpectedly, this morphology change in the undecyl sample also resulted in a higher hydration number compared to the ethyl sample in the liquid water saturated state even though both samples have the same IEC or same concentration of hydrophilic charged groups suggesting differences in the accessibility of the of these charged groups to water. Also, no significant difference in bromide ion conductivity was observed when comparing liquid water saturated to high humidity states in the undecyl samples. This result suggests that a continuous conductive microdomain with water/ion clusters within the PIL microdomains has less impact on the ion conductivity compared to the confinement of water/ion clusters within lamellar PIL microdomains. Overall, the synergistic impact of water/ion clusters and block copolymer morphology on water-assisted ion transport was demonstrated and future studies on this synergistic effect on various block copolymer morphologies and chemistries are highly warranted.

Notes and references

1   1.   M. Hirao, K. Ito and H. Ohno, *Electrochim. Acta*, 2000, **45**, 1291-1294.

2   2.   H. Ohno, M. Yoshizawa and W. Ogihara, *Electrochim. Acta*, 2004, **50**, 255-261.

3   3.   H. Chen, J.-H. Choi, D. Salas-de la Cruz, K. I. Winey and Y. A. Elabd, *Macromolecules*, 2009, **42**, 4809-4816.

4   4.   P. K. Bhowmik, R. A. Burchett, H. S. Han and J. J. Cebe, *Macromolecules*, 2001, **34**, 7579-7581.

5   5.   M. Faraj, E. Elia, M. Boccia, A. Filpi, A. Pucci and F. Ciardelli, *Journal of Polymer Science Part a-Polymer Chemistry*, 2011, **49**, 3437-3447.

6   6.   M. D. Green, J.-H. Choi, K. I. Winey and T. E. Long, *Macromolecules*, 2012, **45**, 4749-4757.

7   7.   R. L. Weber, Y. Ye, A. L. Schmitt, S. M. Banik, Y. A. Elabd and M. K. Mahanthappa, *Macromolecules*, 2011, **44**, 5727-5735.

8   8.   F. S. Bates and G. H. Fredrickson, *Annual Review of Physical Chemistry*, 1990, **41**, 525-557.

9   9.   Y. S. Ye, S. Sharick, E. M. Davis, K. I. Winey and Y. A. Elabd, *Acs Macro Letters*, 2013, **2**, 575-580.

10   10.   N. J. Robertson, H. A. Kostalik, T. J. Clark, P. F. Mutolo, H. D. Abruna and G. W. Coates, *J. Am. Chem. Soc.*, 2010, **132**, 3400-3404.

11   11.   M. Guo, J. Fang, H. Xu, W. Li, X. Lu, C. Lan and K. Li, *Journal of Membrane Science*, 2010, **362**, 97-104.

12   12.   F. Zhang, H. Zhang and C. Qu, *J. Mater. Chem.*, 2011, **21**, 12744-12752.

13   13.   B. Lin, L. Qiu, B. Qiu, Y. Peng and F. Yan, *Macromolecules*, 2011, **44**, 9642-9649.

14   14.   K. Tauer, N. Weber and J. Texter, *Chemical Communications*, 2009, DOI: 10.1039/B912148J, 6065-6067.

15   15.   M. A. Hickner, H. Ghassemi, Y. S. Kim, B. R. Einsla and J. E. McGrath, *Chem. Rev.*, 2004, **104**, 4587-4611.

16   16.   K. A. Mauritz and R. B. Moore, *Chem. Rev.*, 2004, **104**, 4535-4585.

17   17.   K. Schmidt-Rohr and Q. Chen, *Nature Materials*, 2008, **7**, 75-83.

18   18.   Y. A. Elabd and M. A. Hickner, *Macromolecules*, 2011, **44**, 1-11.

19   19.   Y. S. Yang, Z. Q. Shi and S. Holdcroft, *Macromolecules*, 2004, **37**, 1678-1681.

20   20.   L. Chen, D. T. Hallinan, Jr., Y. A. Elabd and M. A. Hillmyer, *Macromolecules*, 2009, **42**, 6075-6085.

21   21.   C. Wang, D. W. Shin, S. Y. Lee, N. R. Kang, G. P. Robertson, Y. M. Lee and M. D. Guiver, *J. Mater. Chem.*, 2012, **22**, 25093-25101.

22   22.   M. Yoonessi, T. D. Dang, H. Heinz, R. Wheeler and Z. Bai, *Polymer*, 2010, **51**, 1585-1592.

23   23.   X. C. Chen, D. T. Wong, S. Yakovlev, K. M. Beers, K. H. Downing and N. P. Balsara, *Nano Letters*, 2014, **14**, 4058-4064.

24   24.   T. J. Peckham and S. Holdcroft, *Advanced Materials*, 2010, **22**, 4667-4690.

25   25.   K. M. Beers and N. P. Balsara, *Acs Macro Letters*, 2012, **1**, 1155-1160.

26   26.   J. Ran, L. Wu and T. Xu, *Polym Chem-Uk*, 2013, **4**, 4612-4620.

27   27.   G. Merle, A. Chairuna, E. Van de Ven and K. Nijmeijer, *Journal of Applied Polymer Science*, 2013, **129**, 1143-1150.

28   28.   D. Chen and M. A. Hickner, *Macromolecules*, 2013, **46**, 9270-9278.

29   29.   M. Tanaka, K. Fukasawa, E. Nishino, S. Yamaguchi, K. Yamada, H. Tanaka, B. Bae, K. Miyatake and M. Watanabe, *J. Am. Chem. Soc.*, 2011, **133**, 10646-10654.

30   30.   T.-H. Tsai, A. M. Maes, M. A. Vandiver, C. Versek, S. Seifert, M. Tuominen, M. W. Liberatore, A. M. Herring and E. B. Coughlin, *Journal of Polymer Science Part B: Polymer Physics*, 2013, **51**, 1751-1760.

31   31.   N. T. Rebeck, Y. Li and D. M. Knauss, *Journal of Polymer Science Part B: Polymer Physics*, 2013, **51**, 1770-1778.

32   32.   J. R. Nykaza, Y. Ye and Y. A. Elabd, *Polymer*, 2014, **55**, 3360-3369.

33   33.   J.-H. Choi, Y. Ye, Y. A. Elabd and K. I. Winey, *Macromolecules*, 2013, **46**, 5290-5300.

34   34.   Y. S. Ye and Y. A. Elabd, *Macromolecules*, 2011, **44**, 8494-8503.

35   35.   D. Salas-de la Cruz, J. G. Denis, M. D. Griffith, D. R. King, P. A. Heiney and K. I. Winey, *Review of Scientific Instruments*, 2012, **83**.

36   36.   P. A. Heiney, *Commision on Powder Diffraction Newsletter* 2005, **32**, 9-11.

37   37.   K. I. Winey, E. L. Thomas and L. J. Fetters, *Journal of Chemical Physics*, 1991, **95**, 9367-9375.

38   38.   S. R. Kline, *Journal of Applied Crystallography*, 2006, **39**, 895-900.

39   39.   P. Schroeder, *Zeit. of Physical Chemistry* 1903, **45**, 75.

40   40.   L. M. Onishi, J. M. Prausnitz and J. Newman, *The Journal of Physical Chemistry B*, 2007, **111**, 10166-10173.

41   41.   W. Y. Hsu and T. D. Gierke, *Journal of Membrane Science*, 1983, **13**, 307-326.

42   42.   A. N. Galatanu, A. L. Rollet, P. Porion, O. Diat and G. Gebel, *Journal of Physical Chemistry B*, 2005, **109**, 11332-11339.

43   43.   A. A. Kornyshev, A. M. Kuznetsov, E. Spohr and J. Ulstrup, *Journal of Physical Chemistry B*, 2003, **107**, 3351-3366.

44   44.   A. Jarosik, S. R. Krajewski, A. Lewandowski and P. Radzimski, *Journal of Molecular Liquids*, 2006, **123**, 43-50.